



UNIVERSITY OF LEEDS

This is a repository copy of *Synchrotron FTIR Mapping of Mineralization in a Microfluidic Device*.

White Rose Research Online URL for this paper:

<https://eprints.whiterose.ac.uk/114434/>

Version: Accepted Version

Article:

Li, S orcid.org/0000-0001-5297-9079, Ihli, J, Marchant, WJ et al. (7 more authors) (2017) *Synchrotron FTIR Mapping of Mineralization in a Microfluidic Device*. *Lab on a Chip*, 17 (9). pp. 1616-1624. ISSN 1473-0197

<https://doi.org/10.1039/C6LC01393G>

(c) 2017, The Royal Society of Chemistry. This is an author produced version of a paper published in *Lab on a Chip*. Uploaded in accordance with the publisher's self-archiving policy.

Reuse

Items deposited in White Rose Research Online are protected by copyright, with all rights reserved unless indicated otherwise. They may be downloaded and/or printed for private study, or other acts as permitted by national copyright laws. The publisher or other rights holders may allow further reproduction and re-use of the full text version. This is indicated by the licence information on the White Rose Research Online record for the item.

Takedown

If you consider content in White Rose Research Online to be in breach of UK law, please notify us by emailing eprints@whiterose.ac.uk including the URL of the record and the reason for the withdrawal request.



eprints@whiterose.ac.uk
<https://eprints.whiterose.ac.uk/>

Synchrotron FTIR Mapping of Mineralization in a Microfluidic Device

Shunbo Li,^a Johannes Ihli,^{†a} William J. Marchant,^a Muling Zeng,^a Li Chen,^b Katia Wehbe,^c Gianfelice Cinque,^c Oscar Cespedes,^d Nik Kapur^e and Fiona C. Meldrum^{a*}

Fourier transform infrared micro-spectroscopy provides an effective means of performing rapid, non-destructive, and label-free analysis of specimens according to their vibrational modes. However, as water absorbs very strongly in the infrared region, analysis of aqueous solutions in transmission mode can suffer from problems with signal saturation. We here describe the fabrication of a novel microfluidic device that overcomes this problem. Devices with channel depths of just 3 μm were constructed from calcium fluoride using photolithography and hot embossing bonding, where calcium fluoride was selected due to its transparency in the IR region. The utility of this device was then demonstrated by employing it to follow the precipitation pathways of calcium sulfate and calcium carbonate using synchrotron FTIR micro-spectroscopy. Importantly, due to the high brightness provided by synchrotron radiation, and the fact that the reacting ions (HCO_3^- , CO_3^{2-} and SO_4^{2-}) and the different mineral polymorphs all have finger print spectra in the measured IR range, this method can be used to acquire time-resolved, hyperspectral maps of the mineral particles formed within the sample cell, and then study the interaction and evolution of particles. The data provide new insight into the formation pathway of a population of crystals in confined volumes, and demonstrate that this in situ, real-time detection system provides a powerful tool for studying crystallization processes.

Introduction

Coupling on-chip analytical techniques with microfluidic devices provides an attractive means of performing chemical and biological analyses.¹ Small volumes of reagents can be readily analyzed, and these flow-based systems are ideally-suited to making sensitive, spatiotemporal-resolved measurements. Droplet based microfluidics² can provide further control over the reaction environment, and ultimately promise the ability to perform and analyze reactions based on a small number of molecules only. The most common *in situ* techniques used to achieve on-chip analyses include electronic signaling such as impedance measurements,³ imaging using optical and fluorescence microscopy,⁴ Raman⁵ and Fourier Transform-Infrared (FTIR) Spectroscopy.⁶ More specialized techniques such as small angle scattering (SAXS)⁷ are also beginning to be explored. In all cases, as only small reaction volumes are being sampled, it is essential that the selected characterization technique is sufficiently sensitive to deliver the information required. In addition to determining the average properties of a reacting solution, it is often desirable to obtain spatially-resolved analytical data. This is seen, for example, in the need to image the interactions of a cell with its environment,⁸ or to study the activity of a catalytic particle.⁹ With their ability to create well-defined, localized reaction environments, microfluidic systems are also very well-suited to this task, where this places further demands on the applied characterization technique.

FTIR micro-spectroscopy offers an attractive means of achieving this goal as it is non-destructive, sensitive and rapid. Compared to conventional FTIR microscopy,¹⁰ which typically uses global sources, synchrotron FTIR is 100–1000 brighter in the mid-farIR. This allows smaller regions to be analyzed, which allows chemical information to be acquired in the form of IR absorption maps.¹¹ Due to the strong absorption of water in the IR region, a further requirement of FTIR analysis of aqueous-based systems is that they are conducted in cells that offer short path lengths to avoid problems with signal saturation. Microfluidic devices are well-suited to this requirement and recent research exploring their combination with IR spectroscopy to study drug release and catalytic processes has been reported.¹² ¹³ Most of the chips described have been created by the top-down etching of CaF₂ crystals to generate the required microchannels.^{14, 15} Calcium fluoride provides a transparent window in the mid-IR range, while control of the channel depth minimizes the absorption of the IR radiation by the water. However, these etching methods usually employ strong acids, and are therefore experimentally cumbersome.

This article describes the fabrication of a novel, calcium fluoride based microfluidic device for the time-resolved study of solution-based processes using time-resolved synchrotron FTIR micro-spectroscopy.

Rather than using top-down etching, we employ a common photoresist in combination with UV lithography to define the channels in one CaF₂ plate. The patterned CaF₂ plate is then bonded to a second unpatterned plate by thermal compression. This bottom-up method has many advantages including ease of fabrication, thickness control, rapid preparation and reliability. We then employ this device to study the dynamic process of crystallization, where our focus is on the important mineral systems calcium sulfate and calcium carbonate. We show that FTIR micro-spectroscopy can provide a unique means of investigating the precipitation pathways of these inorganic materials, such that we can image the developing population of mineral particles, mapping the polymorphs within the reaction cell. The strength of this approach is demonstrated by analysis of the complex calcium carbonate system, where mapping of the reaction chamber using FTIR spectroscopy enables us to quantify the proportions of the different polymorphs present at different times and positions within the mapping region. Our data show that amorphous calcium carbonate (ACC) transforms into crystalline vaterite and calcite over time, and that this process proceeds more slowly within the confines of the microfluidic device as compared with bulk solution. It is envisaged that this microfluidics-based system could be used to study a wide range of dynamic processes such as the interaction of cells with their environments.

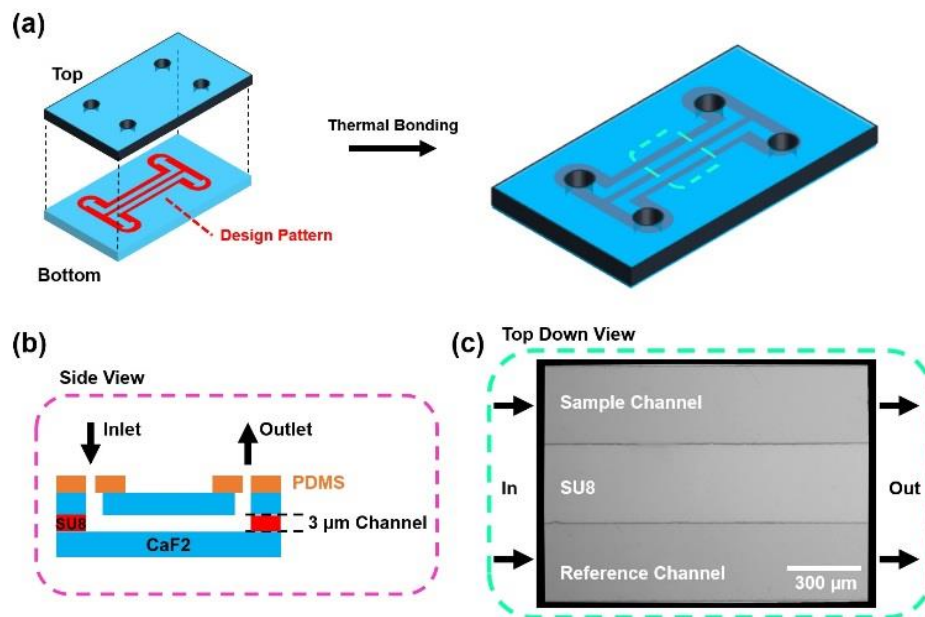


Fig. 1. Illustration of the calcium fluoride microfluidic devices and the fabrication method employed. (a) Photolithography methods were used to create channels on one CaF₂ plate (bottom), which was then bonded to a second CaF₂ plate (top) in which holes for inlets and outlets had been drilled. The device was then assembled through thermal bonding. (b) Side view through the device. Channels are 3 μm in height and the in/outlets were sealed after loading. (c) Optical micrograph of the assembled device, where a top down view is presented. The device possesses two channels, corresponding to the sample and reference, which are each 300 μm in width.

Materials and Methods

Materials

Calcium chloride, sodium sulfate, ammonium carbonate, sodium carbonate and L-Aspartic acid (sodium salt) were obtained from Sigma Aldrich. CaF₂ crystal plates with size of 1 cm x 1 cm x 1 mm (L x W x H) and inlets and outlets holes with diameter of 1 mm were provided by Crystran Ltd. (Dorset, England). PDMS (Sylgard 184 Elastomer Kit) was obtained from Dow Corning and EVO-STIK epoxy glue was purchased from Bostik (UK).

Preparation of Microfluidic Devices

Microfluidic Chips were prepared using standard photolithography processes,¹⁶ where a schematic diagram of a prepared microfluidic chips and the bonding process used are shown in Fig. 1. Briefly, SU8 2002 was spin-coated on a calcium fluoride crystal plate to a thickness of 3 μm using a spin speed at 1000 rpm. The coated crystal was then soft-baked at 65 °C for 3 min and hard-baked at 95 °C for 5 min. Subsequent UV exposure was conducted using a MJB3 mask aligner (Karl Suss, Coventry, UK) at an exposure energy of 110 mJ cm⁻² and the plate was developed in EC solvent for 1 min. Thermal bonding between the photolithography patterned substrate and an unpatterned CaF₂ substrate drilled with four holes was conducted using an AWB aligner (AML, Didcot, UK), by placing the two aligned substrates on the bottom table of the wafer bonder. The chamber was closed and a vacuum was applied below 2.67 x 10⁻⁵ mbar. The table was then heated to a temperature of 120 °C and a force of 1 kN was applied across the substrates between the upper and lower clamp table for 10 minutes to complete the bonding. The force was then removed and the tables were allowed to cool to room temperature prior to removal of the bonded substrates. The substrates were then sealed with epoxy glue at the edges to further support the bonding. The bonding strength was tested and no leakage was found under pressure of 1 bar, which is sufficient for liquid injection. Due to the brittle nature of the CaF₂ windows, the inlet and outlet tubes were attached to the microfluidic device via PDMS blocks punched perforated with 1 mm holes and glued to the CaF₂ plates (shown in Fig. 1b of the side view). Two parallel microchannels, one for sample loading and the other one for background reference, were designed (Fig. 1c). After solution injection, the inlet and outlet were covered by PDMS slabs to slow down evaporation, such that minimal evaporation occurred over 3h. The microfluidic chips generated have channel heights of only 3 μm, widths of 300 μm and lengths of 4600 μm, where this corresponds to a reaction volume of about 4.3 nL. It is noted that the channel height could be varied as desired by simply choosing appropriate photoresist and spin speeds.

Crystallization Experiments

Crystallization within the Microfluidic Device

Solutions were prepared in deionized (DI) water and were mixed prior to injection into the microfluidic chip using a syringe. Crystallization of amorphous calcium carbonate (ACC) was studied within the microfluidic device by initially preparing a suspension of ACC in bulk solution and then injecting it into the chip using a syringe. The whole chip was then closed without fluid flow during spectrum acquisition. The ACC was prepared by combining equal volumes (100 μL) of 500 mM CaCl_2 and Na_2CO_3 solutions and then diluting this suspension with 200 μL DI water to dilute the precipitates for easy injection into the microfluidic chip. Precipitation of calcium sulfate within the microfluidic chip was achieved by preparing a solution of concentration 125 mM CaCl_2 and Na_2SO_4 and 25 $\mu\text{g mL}^{-1}$ aspartic acid, where the aspartic acid was added to retard the reaction. Set-up of the chip for analysis, optimization of the synchrotron beam and measurement of the background spectra then take 20 min, such that data describing crystal growth are acquired after 20 min.

Crystallization in Bulk Solution

CaCO_3 was also precipitated in bulk in order to investigate the effects of confinement (as offered by the microfluidic channels) on the crystallization process. Equal volumes (500 μL) of 500 mM CaCl_2 and Na_2CO_3 solutions were combined in a centrifuge tubes and 1 mL DI water was then added to the CaCO_3 suspension. Crystals were collected at different times by filtration through a filter membrane with 100 nm pore size.

Preparation of CaCO_3 Reference Samples

Dry powders of ACC, vaterite and calcite were also prepared as control samples, and their FTIR spectra were recorded. ACC was produced by mixing equal volumes (0.5 mL) of 1 M $(\text{NH}_4)_2\text{CO}_3$ and CaCl_2 at 4 $^\circ\text{C}$, followed by immediately filtering through a 100 nm Isopore GTTP membrane filter (Millipore), washing with ethanol and drying in a vacuum chamber for 1 h. Vaterite was prepared by adding equal volumes (4.95 mL) of 100 mM CaCl_2 and 100 mM $(\text{NH}_4)_2\text{CO}_3$ to 80 mL DI water at 30 $^\circ\text{C}$, followed by stirring for 15 min. The precipitate was then filtered, washed with ethanol and dried under vacuum for 1h. Calcite was prepared using the ammonia diffusion method.¹⁷ In detail, a Petri dish containing 20 mL of 10 mM CaCl_2 solution was placed in a sealed desiccator along with a dish containing $(\text{NH}_4)_2\text{CO}_3$ powder for 1h. The precipitate formed was then isolated by filtering, washing and drying.

Synchrotron FTIR Micro-spectroscopy

Data were collected at beamline B22 at the Diamond Light Source (Oxford, UK) using a Bruker Vertex 80 V FTIR spectrometer coupled to a continuum IR microscope, and synchrotron light as the infrared

source. The microscope was equipped with a 36x objective, a motorized high precision x–y mapping stage, an adjustable rectangular aperture, and a liquid N₂-cooled MCT high sensitivity detector of size 50 × 50 μm². The spectral range of the detector was 4000–500 cm⁻¹, the spectral resolution was 2 cm⁻¹ and the IR microscope stage was raster-scanned through the area with a step size of a 5 μm. The acquisition conditions were defined in transmission mode, where sites for analysis were selected using the microscope in visible microscopy mode; the incident beam size after passage through the aperture used to obtain IR spectra was approximately 10 × 10 μm². Spectrum mapping was performed of 10 × 10 arrays of step size 5 μm, using 16 scans per pixel, corresponding to a total scanning time of approximately 10 min. Time-resolved mapping was performed every 15 min for all experiments. The mapping area was chosen near the centerline of channel to get away of edge effects as much as possible.

In making measurements, it was also important to record background spectra of the device alone (no solution). The CaF₂ crystals employed have a clear window (transmission greater than 92%) from 1250 cm⁻¹ to 4000 cm⁻¹ (Fig. S1) which correspond to wavelengths of 8 μm and 2.5 μm respectively. The main peaks of the CaCO₃ polymorphs are located between 1375 cm⁻¹ to 1500 cm⁻¹, where the CaF₂ has very good transmission. However, the principal peak corresponding to the sulfate ions occurs at 1112 cm⁻¹, which falls within a regime – between 1250 cm⁻¹ (8 μm) and 1000 cm⁻¹ (10 μm) – in which the transmission decays. This effect could be compensated for by recording a background signal at the reference channel, such that a clear, sharp peak could be obtained for the sulfate ions. CaF₂ crystals are therefore suitable materials for constructing FTIR microfluidic chips comprising parallel channels.

Data Processing Methods

All of the experimental IR spectra were acquired using Bruker OPUS 7.2 software and were analyzed using Matlab R2013a (MathWorks, Natick, MA, USA). The chemical maps of calcium carbonate were generated by calculating the area under the carbonate absorption peak from 1250 cm⁻¹ to 1550 cm⁻¹ (represented by *A*) at each position in the mapped area. This represents the total amount of carbonate (from all phases) present. Each individual FTIR spectrum was also analysed to determine the contributions from the different calcium carbonate polymorphs. This was achieved using a linear combination fitting as described below. The ratio of different polymorphs of calcium carbonate at different positions in the field of analysis was determined by analyzing the shape of the experimentally-recorded absorption peak, where this is a superposition of the contributions from the amorphous calcium carbonate (ACC), vaterite and calcite present. By trialing different proportions of these three components and comparing with the experimental data, the composition of the

precipitates can then be determined. Firstly, basic components for each of these three phases were extracted from the synchrotron FTIR data, and the absorption peaks were normalized to 1 and represented by Y_{ACC} , Y_{Vat} and Y_{Cal} respectively. The fraction of ACC present was defined as a , which could take values between 0 to 1 with an interval of 0.01, while the fraction of vaterite was defined as b and could take values from 0 to $(1 - a)$ with an interval of 0.01. The fraction of calcite therefore corresponds to $c = 1 - a - b$. The deviation of the calculated “test” spectrum (generated as a superposition of peaks from calcite, vaterite and ACC) from the experimental peak was calculated as:

$$Dev = \sum_i |y_{FTIR} - Pe \cdot (a \cdot Y_{ACC} + b \cdot Y_{Vat} + c \cdot Y_{Cal})| \quad (1)$$

, where y_{FTIR} and Pe are the acquired spectrum and absorption peak for each point in the 10×10 mapping array. As the peak values are not all the same, all of the data have to be re-normalized according to the total carbonate absorption peak to explicitly show the amounts of precipitants. The summation () was conducted through the carbonate main peak between 1250 cm^{-1} and 1550 cm^{-1} . The minimum deviation was saved when going through all the values of a and b . Finally, the quantities of the three polymorphs at each map point could be obtained as $A \cdot a$, $A \cdot b$ and $A \cdot c$ where, A is the area under the carbonate absorption band. This number therefore also reflects the amount of material present at different points in the cell.

Results and Discussions

Rationale for Microfluidic Device Design

Microfluidic devices comprising anodic bonded Si/Pyrex or fusion bonded Si/Si^{18, 19} can be manufactured to create well-defined channels using standard processes, offer good stability to harsh chemicals, and are stable over a wide temperature range and at higher pressures.¹⁸ However, devices with thicknesses of a few hundred microns also have significant reflection losses,²⁰ plus being not transparent to the visible microsample centring becomes an issue, and Pyrex glass has Si-O absorption bands which interfere with ones of many samples. CaF₂, in contrast, has a very high transmission coefficient (Fig. S1) which facilitates study of crystallization under normal environments in confinement.

The microfluidic chip was designed to have two parallel microchannels, one of which is used to load the reaction solution and the other is used as background reference. These two channels are located close to each other for ease of operation; the reference measurement can then be made by moving the chip just 300 – 600 μm in one direction. This measurement provides an essential background measurement which can be subtracted from the reaction solution data. The channel height and width were chosen to be 3 μm and 300 μm respectively to minimize IR absorption by the water (a channel

height below 10 μm is desirable) and to have an appropriate mapping area. The importance of the small channel height in our experiments was confirmed by measuring the absorption spectra of water in a liquid cell with thickness of 25 μm and in our device, which has a path-length of 3 μm . The saturation is severe for the liquid cell, while unsaturated spectra were recorded using our microfluidic chip (Fig. S2). Microfluidic chips with well-defined, smaller channel heights are therefore required. Further, as compared to the use of direct etching methods to create channels on CaF_2 crystals, our technique is easy, fast and precise.

Precipitation of Calcium Sulfate in the Microfluidic Chip

Calcium sulfate is an important mineral in the environment, where gypsum ($\text{CaSO}_4 \cdot 2\text{H}_2\text{O}$) is the stable polymorph under ambient conditions.²¹ As the sulfate ion has its principal FTIR band near 1100 cm^{-1} , our methodology can be used to monitor the formation of gypsum. Reactions were carried out by injecting a supersaturated solution of calcium sulfate containing a low concentration of aspartic acid into the microfluidic chip. The aspartic acid retards the reaction and stops precipitation from occurring while setting up the system. The composition of the reaction solution in the microfluidic chip was mapped using a 10×10 array, with a step size of 5 μm , and conducting 16 scans at each point. The sulfate peak at 1100 cm^{-1} was seen to decrease during acquisition of the FTIR maps. However, no bands corresponding to gypsum were recorded in this mapping area. After 50 min reaction time, the observation area was changed to a neighbouring position $\approx 200\text{ }\mu\text{m}$ away, where a single large gypsum crystal was identified. The relatively low supersaturation of CaSO_4 was employed, and the small volume of solution in the chip ($\approx 4.3\text{ nL}$) is such that the product crystals are distributed with typical separations of $\approx 200\text{ }\mu\text{m}$. A randomly-selected area of $50 \times 50\text{ }\mu\text{m}^2$ therefore cannot be guaranteed to feature a crystal. Use of a microfluidic chip with localized rooms that define the location of crystal growth would provide an elegant solution to this problem.²²

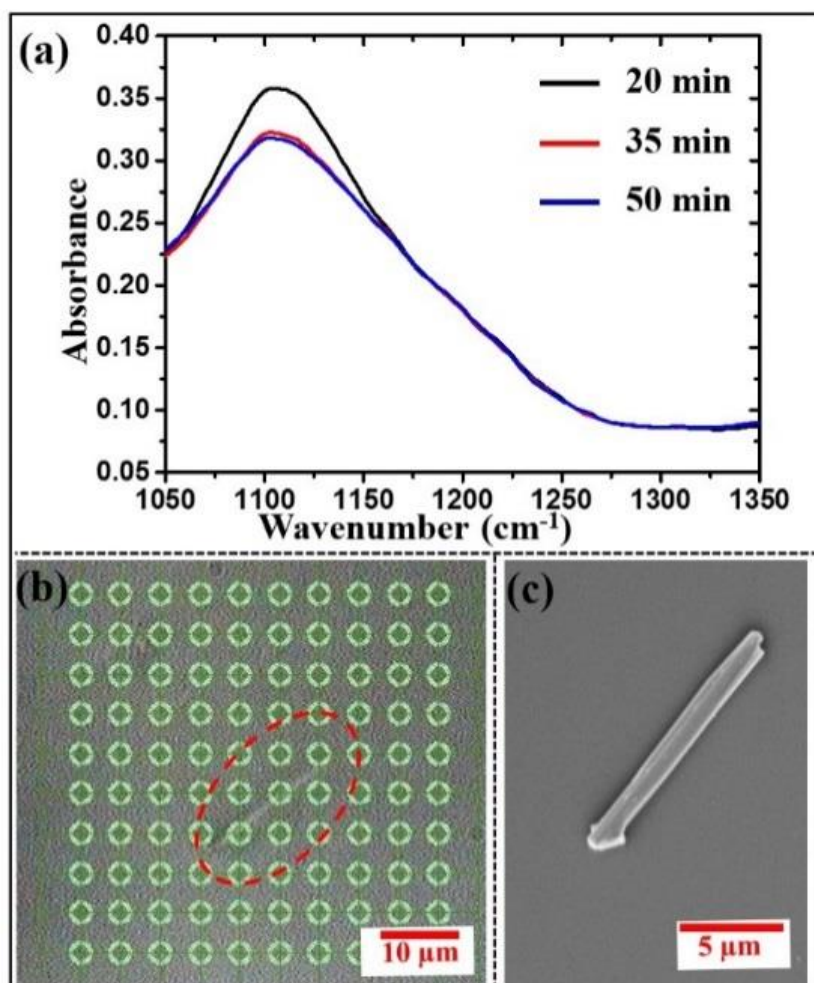


Fig. 2 Precipitation of gypsum from a solution of composition 125 mM CaCl₂ and Na₂SO₄ and 25 μg mL⁻¹ aspartic acid, as monitored using synchrotron FTIR imaging. (a) The averaged signal for all the 100 points at 20, 35 and 50 min. (b) Optical micrograph of a gypsum crystal located about 200 μm from the mapping area (highlighted by red-dashed line). (c) SEM image of a gypsum crystal prepared in bulk solution under the reaction conditions.

The averaged FTIR bands recorded for all 100 positions at times of 20 min, 35 min and 50 min were calculated using Matlab and the results are shown in Fig. 2a. As no crystal precipitated in this region, the solution concentration was taken as uniform throughout. It is clearly seen that the sulfate peak drops significantly between 20 and 35 min, but then remains stable between 35 and 50 min. This shows that gypsum precipitation is complete within 35 min under these reaction conditions. Fig. 2b shows an optical micrograph of a gypsum crystal located about 200 μm away from the mapping area, while Fig. 2c is an SEM image of a gypsum crystal formed from a bulk solution of identical composition. These studies demonstrate that calcium sulfate precipitation from solution can be successfully monitored using *in situ* FTIR measurements of the reaction solution.

Monitoring the Evolution of CaCO₃ Crystals in Confinement

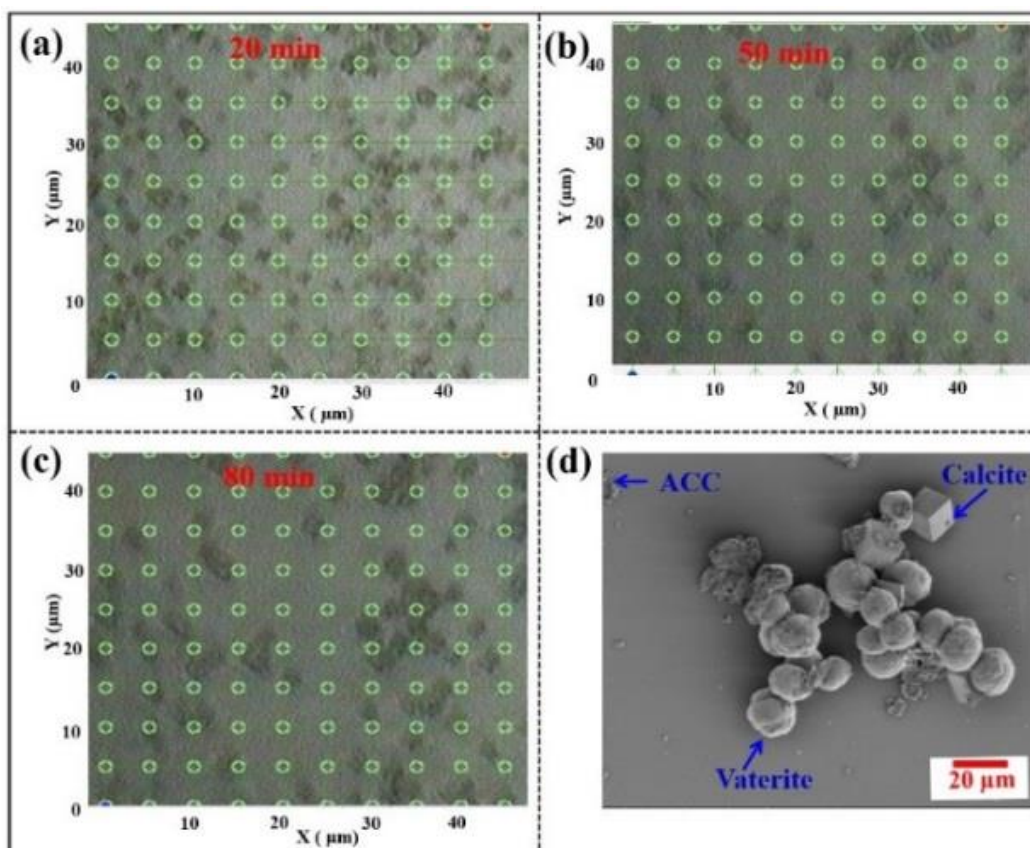


Fig. 3 Images of calcium carbonate particles. (a-c) Optical micrographs of the mapped areas (conducted as 10 × 10 arrays), recorded at 20 min, 50 min and 80 min. (d) SEM image of CaCO₃ particles formed from a bulk solution containing 250 mM CaCl₂ and Na₂CO₃ after 20 min. The polymorphs in (d) were identified and confirmed by Raman microspectroscopy (Fig. S3).

The precipitation of calcium carbonate from solution is complex, due to the existence of three anhydrous polymorphs – vaterite, aragonite and calcite – which can all show substantial stability under ambient conditions. CaCO₃ also frequently precipitates as a hydrated amorphous phase (amorphous calcium carbonate, ACC), which subsequently transforms into more stable crystalline phases.²³ IR micro-spectroscopy within the microfluidic device used here therefore provides a unique opportunity to image the transformation of ACC to crystalline polymorphs, and to investigate how this process occurs within constrained volumes.

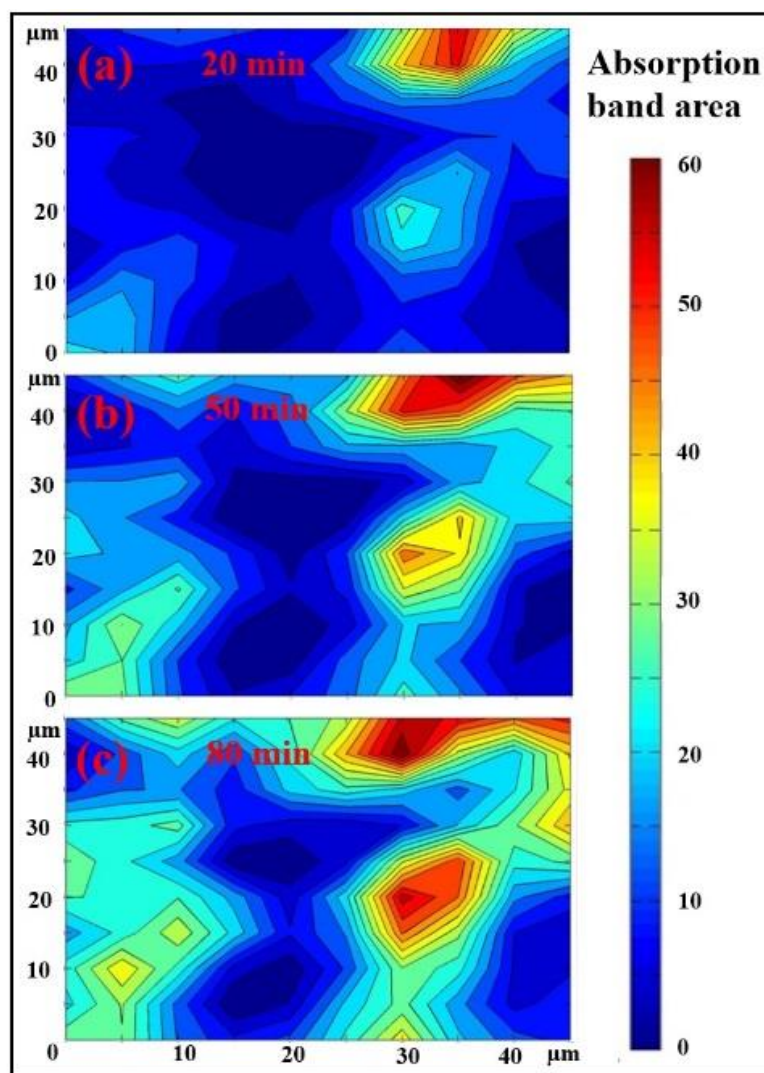


Fig. 4 Integration of the area under the carbonate absorption bands recorded at different positions in the cell at (a) 20 min, (b) 50 min and (c) 80 min

A suspension of ACC precipitates was injected into the microfluidic chip, its inlets and outlets were sealed using PDMS, and a series of maps and optical images were recorded with time. Optical images of the mapping area are shown in Fig. 3a-c, where these correspond to times of 20, 50 and 80 min. These images demonstrate that the distribution of crystals changes significantly between (a) and (b), but then remains very similar between (b) and (c). The amount of crystalline material does continue to increase after 50 min, however, where this can be seen in the increase in FTIR absorption. FTIR maps were created by scanning a square array of 100 points, the centers of which are indicated by the circles on the images. The raw data obtained in the FTIR measurements are shown in Fig. S4, where the individual graphs show the entire time series recorded (from 20 to 95 min, with 15 min intervals). The plots demonstrate that the amount of mineral increases with time and that there is a systematic change in polymorph. However, it is difficult to immediately determine how the population of crystals

present within the mapping area evolves with time from such a large set of plots. Key information – including the shapes and heights of the FTIR bands – were therefore extracted to generate a clear picture of the development of the polymorphs of the CaCO_3 particles, and how individual particles affect the growth of their neighbours.

Information about the quantities of precipitates present at each point in the mapped area is contained in the area under the carbonate FTIR absorption band, and reflects all polymorphs present. This was evaluated by integrating the band between 1250 cm^{-1} and 1550 cm^{-1} . Thicker individual particles or aggregates of particles necessarily yield a stronger FTIR absorption band due to the greater path-length. This data is displayed in Fig. 4 as a color map of the areas shown in Fig. 3a – 3c, where red represents higher absorption signals and blue lower absorption signals. The amount of crystalline material increases with time, as is clearly show in Fig. 4a – 4c.

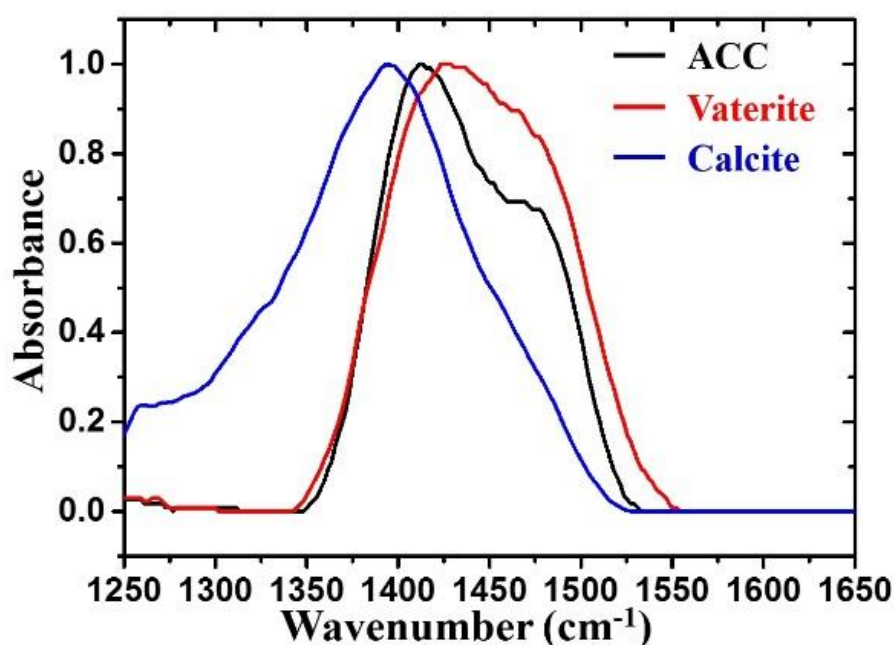


Fig. 5 Synchrotron FTIR spectra for ACC, vaterite and calcite. The curves were normalized to have the same absorption at their maxima.

The data was also processed to determine which polymorphs were present, and how their locations changed with time. The principal FTIR bands arising from the carbonate ions in the different calcium carbonate polymorphs have characteristic positions and line shapes, as is shown in Fig. 5 (where the spectra are normalized for easy comparison of the band shapes). The band for ACC is asymmetric and comprises a main peak at 1410 cm^{-1} and a shoulder at 1475 cm^{-1} . Calcite exhibits a sharp peak at $\approx 1394\text{ cm}^{-1}$ that is slightly asymmetric, while the vaterite band appears broad and highly asymmetric, and comprises a main peak at 1425 cm^{-1} and a shoulder at 1475 cm^{-1} . The different CaCO_3 polymorphs

can therefore be easily distinguished using FTIR. It is noted that the peak positions recorded in the microfluidic devices are slightly shifted as compared with data recorded from powders using ATR FTIR (Fig. S5), where ACC has a peak at 1404 cm^{-1} , vaterite has a broad peak at $1395\text{-}1471\text{ cm}^{-1}$ and calcite has a peak at 1392 cm^{-1} . This can be attributed to differences in particle sizes, where samples for ATR FTIR are typically ground and analyzed as dry powders. This can lead to changes in the positions and intensities of the vibrational bands (the Christiansen effect).²⁴

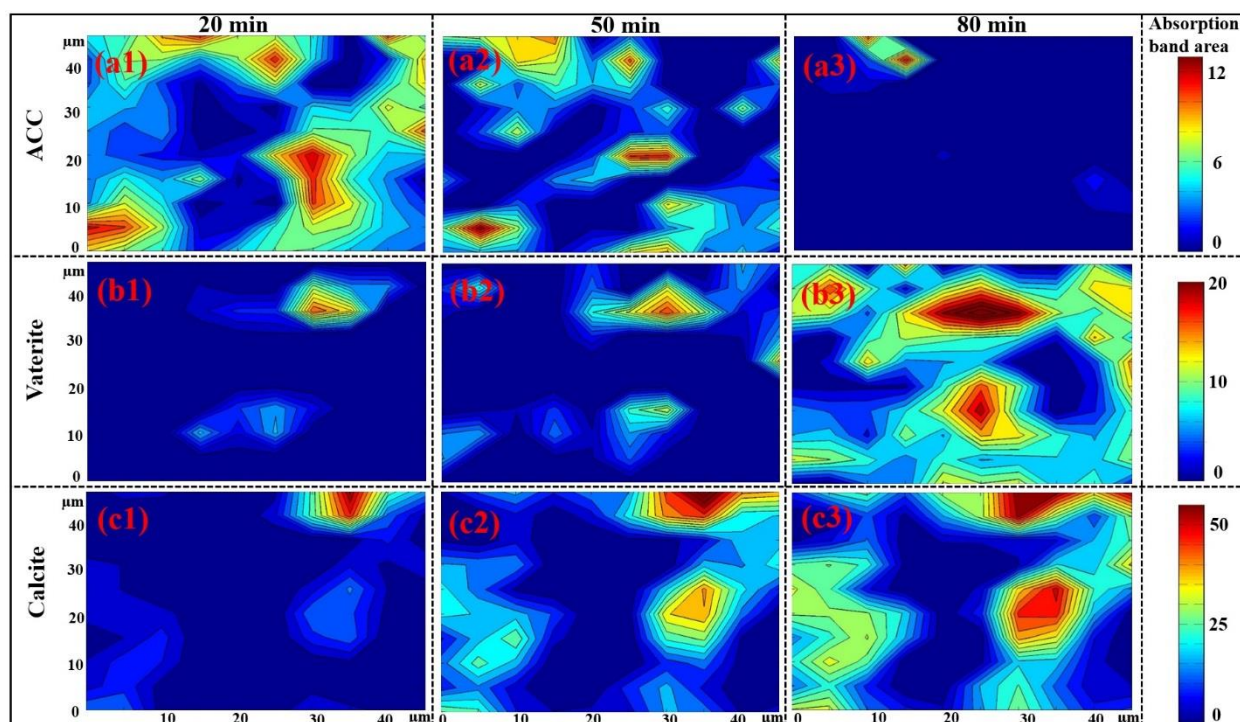


Fig. 6 The evolution of (a) ACC, (b) vaterite and (c) calcite within the microfluidic chip with time. The scale on the right shows the absorption band area relative to the total carbonate content in Fig.4.

The FTIR spectra shown in Fig. 5 were used as references to determine the relative proportions of the calcium carbonate polymorphs present in the microfluidic devices at different reaction times, where this was performed using the data processing protocols described previously. The evolution of ACC, vaterite and calcite within the mapping area is shown in Fig. 6. This Figure shows the fraction of the different phases present at each point in the cell, where this was determined by multiplying the fraction of ACC, vaterite and calcite present by the area under the carbonate absorption band at each point ($A \cdot a$, $A \cdot b$ and $A \cdot c$, as explained in the “Data processing methods”). This then also allows the amount of material present at different points in the cell to be compared. The interval between the sequential maps shown here is 30 min.

Looking first at the changes in the population of ACC particles with time, Fig. 6a1 shows that significant

amounts of ACC are present at early times (red areas), and decrease with time. The red areas undoubtedly correspond to aggregates of particles, as individual particles of ACC are typically small (< 100 nm). There is a significant decrease in the amount of ACC present between 20 and 50 min, and little ACC remains by 80 min. The data also shows that there is a dynamic exchange between ACC and the more stable crystalline polymorphs vaterite and calcite, where crystals grow from the reservoir of ACC. The quantities of both vaterite and calcite in these systems increase with time (Fig. 6b1 - b3 and Fig. 6c1 - c3), as is shown by an increase in the absorption and size of the domains associated with crystals. The proportion of vaterite is higher than calcite after 80 min (Fig. 6b3 and 6c3).

Effects of Confinement on Calcium Carbonate Precipitation

It is also valuable to compare the progress of ACC transformation within the confines of the microfluidic device with that in bulk solution. CaCO₃ was therefore precipitated under identical conditions in bulk solution, and the solution appeared cloudy at 20 min (the starting point for IR measurements) and clear after 30 min (Fig. S6), due to sedimentation of large crystals. Powder FTIR and XRD analysis of the precipitates produced after 20 min showed that significant quantities of vaterite and calcite were present, together with some ACC (Fig. 7), where this was consistent with SEM images (Fig. 3d and Fig. S7a). It is noted that the main peaks of vaterite and calcite overlap to give a broad peak from 1400 cm⁻¹ – 1500 cm⁻¹ in Fig. 7a. No ACC was detected using FTIR after 35 min since ACC is a hydrated phase and no water was presented after 35 min as shown in Fig. 7a. By comparison, large amounts of ACC were still present within the microfluidic device after 50 min and small quantities were still detected after 80 min (Fig. 6 (a3)).

These data clearly show that confining ACC within the channels of the microfluidic cell greatly increases its lifetime. It is now recognized that precipitation reactions proceed significantly more slowly in confinement, and that variations in polymorph stability,²⁵⁻³² crystal orientation,^{33, 34} morphology^{35, 36} and single crystal/ polycrystalline character^{37, 38} can occur, even in micron-scale environments. Indeed, a wide range of materials including calcium carbonate,^{25, 26, 37} calcium phosphate,^{27, 33} calcium oxalate,²⁹ calcium sulfate,³⁹ potassium ferrocyanide³² and organics such as glycine⁴⁰ have shown a stabilization of metastable phases in small volumes. Although the origin of this effect is as yet unclear, a number of factors which are likely to contribute. For example, impurities (that can act as nucleants) are often eliminated from small volumes, which results in an increase in the lifetime of metastable phases.²⁵ Crystallisation processes that proceed via the dehydration/ hydration of metastable phases or via the aggregation of precursor particles may also be retarded within small volumes.^{26, 27, 39} As a potential general mechanism, crystals formed within confined

volumes are fixed in position, and thus only experience their local environments. This is a major distinction from bulk systems in which crystals are mobile and interact with many other crystals and impurities. Transport of material to a growing crystal, particularly through convection, will also be greatly reduced in confinement, which will also extend the lifetime of the metastable phase.

Imaging Crystallization Processes

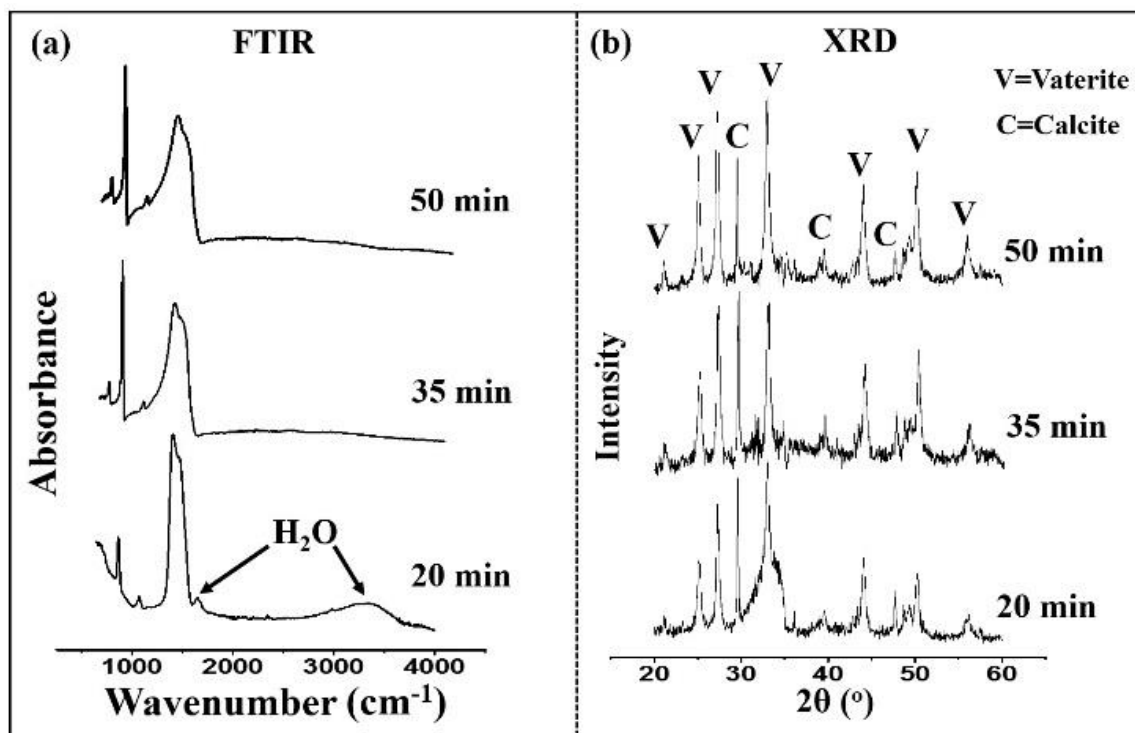


Fig. 7 (a) FTIR spectra and (b) powder XRD diffractograms of calcium carbonate precipitates prepared in bulk solution and isolated after 20 min, 35 min, and 50 min. V corresponds to vaterite and C to calcite.

The study of crystallization processes has benefitted enormously from imaging techniques. From traditional optical microscopy methods, which enable the growth of micron-scale crystals to be studied *in situ* in solution, to scanning probe microscopy, with the ability to image growing crystals with atomic resolution under optimal conditions, has opened the door to a new understanding of crystal growth mechanisms.⁴¹⁻⁴⁵ Developments in electron microscopy have also provided significant new insights into crystallization processes. High resolution cryo-TEM (transmission electron microscopy) can provide snapshots of the precipitates present at key time-points in the reaction,⁴⁶ while liquid-phase TEM is opening the door to the real-time study of the nucleation, growth and assembly of nanoscale particles in solution.^{47, 48} Sophisticated synchrotron-based X-ray diffraction

imaging methods can be used, for example, to image both the growth mechanism and strain development within individual calcite crystals.^{49, 50}

Determination of the origin of confinement effects on crystallization processes, however, would benefit enormously from the ability to image the changes in both the mineral phases present *and* the reaction solution. The development of a microfluidic device that facilitates FTIR spectroscopic imaging of the developing crystals and the solution phase surrounding them provides a potential route to achieving this goal. Both of the minerals studied here – calcium sulfate and calcium carbonate – have low solubilities in water, such that the spectroscopic sensitivity available to us was not sufficient to image concentration gradients in the solution. However, for study of alternative systems, and with inevitable improvements in instrumentation, this goal is likely to become achievable.

Conclusions

With its high intensity and polarized nature, synchrotron FTIR microscopy is attracting increasing attention for the analysis of a wide range of processes in solution including heterogeneous catalysis,^{51, 52} electrochemical reactions⁵³ and flow through porous media.⁵⁴ Such studies rely on the availability of suitable sample cells, where these must possess windows that have high transparency in the IR, and for FTIR of aqueous solutions (or other strongly absorbing solvents), they should exhibit a short path length such that the IR signal does not become saturated. The sample cell must also be straightforward to fill, empty and clean. In the work described here, we have developed a novel microfluidic chip design that meets all of these requirements, and which can be readily tailored according to the needs of an individual experiment. We then used this device to study the precipitation of two important crystal systems – calcium sulfate and calcium carbonate. Thanks to differences in the positions and shapes of the carbonate absorption bands of the different calcium carbonate phases, we were able to determine the proportions of each phase present at different points in the cell and monitor the evolution of amorphous calcium carbonate (ACC) to vaterite and calcite. A further feature of the sample cell employed here is that the 3 μm chamber height selected also enabled us to study the effects of confinement on the precipitation of the inorganic solids, where this has parallels to the many important environmental, biological and technological processes that occur in small volumes. The lifetimes of the ACC and vaterite were extended within the microfluidic cell, where the suppression of convection in this environment may contribute to this effect. It is envisaged that this microfluidics-based system could be used to study many dynamic processes as diverse as heterogeneous catalysis, crystallization and the interaction of cells with their environments, where use of an FPA detector could give access to faster analysis times, as required.

Acknowledgements

We thank Diamond Light Source for access to the MIRIAM beamline, B22, (proposal number: SM12717-1) that contributed to the results presented here. The authors would like to thank Yi-Yeoun Kim for fruitful discussions. This project was supported by Engineering and Physical Sciences Research Council (EPSRC) grants EP/L015005/1 (SL and FCM) and EP/N002423/1 (MZ and FCM), and an EPSRC Leadership Fellowship EP/H005374/1 (FCM and JI).

Notes and references

1. K.-I. Ohno, K. Tachikawa and A. Manz, *Electrophoresis*, 2008, **29**, 4443–4453.
2. M. Srisa-Art, A. J. deMello and J. B. Edel, *Anal. Chem.*, 2007, **79**, 6682-6689.
3. T. Sun and H. Morgan, *Microfluidics and Nanofluidics*, 2010, **8**, 423-443.
4. S. Li, Z. Ye, Y. S. Hui, Y. Gao, Y. Jiang and W. Wen, *Biomicrofluidics*, 2015, **9**, 054115.
5. A. F. Chrimes, K. Khoshmanesh, P. R. Stoddart, A. Mitchell and K. Kalantar-Zadeh, *Chem Soc Rev*, 2013, **42**, 5880-5906.
6. K. L. Chan and S. G. Kazarian, *Anal Chem*, 2012, **84**, 4052-4056.
7. F. Schwemmer, C. E. Blanchet, A. Spilotros, D. Kosse, S. Zehnle, H. D. T. Mertens, M. A. Graewert, M. Rössle, N. Paust, D. I. Svergun, F. V. Stetten, R. Zengerle and D. Mark, *Lab Chip*, 2016, **16**, 1161–1170.
8. K. Wehbe, A. Travo, S. Eimer, G. Cinque, E. Barron, G. Déléris and I. Forfar, *Analytical Methods*, 2013, **5**, 6925.
9. E. C. V. Eschenroeder, A. Turrina, A. L. Picone, G. Cinque, M. D. Frogley, P. A. Cox, R. F. Howe and P. A. Wright, *Chemistry of Materials*, 2014, **26**, 1434-1441.
10. K. L. Chan, X. Niu, A. J. de Mello and S. G. Kazarian, *Lab Chip*, 2010, **10**, 2170-2174.
11. W. D. Duncan and G. P. Williams, *Appl Opt*, 1983, **22**, 2914 – 2923.
12. A. V. Ewing, G. S. Clarke and S. G. Kazarian, *Biomicrofluidics*, 2016, **10**, 024125.
13. I. P. Silverwood, N. Al-Rifai, E. Cao, D. J. Nelson, A. Chutia, P. P. Wells, S. P. Nolan, M. D. Frogley, G. Cinque, A. Gavriilidis and C. R. Catlow, *The Review of scientific instruments*, 2016, **87**, 024101.
14. B. Lehmkuhl, S. D. Noblitt, A. T. Krummel and C. S. Henry, *Lab Chip*, 2015, **15**, 4364-4368.
15. T. Pan, R. T. Kelly, M. C. Asplund and A. T. Woolley, *Journal of Chromatography A*, 2004, **1027**, 231-235.
16. S. Li, M. Li, Y. S. Hui, W. Cao, W. Li and W. Wen, *Microfluidics and Nanofluidics*, 2012, **14**, 499-508.

17. J. Ihli, P. Bots, A. Kulak, L. G. Benning and F. C. Meldrum, *Adv. Func. Mater.*, 2013, **23**, 1965-1973.
18. S. Marre, A. Adamo, S. Basak, C. Aymonier and K. F. Jensen, *Ind. Eng. Chem. Res.*, 2010, **49**, 11310–11320.
19. J. S. Moore, C. D. Smith and K. F. Jensen, *React. Chem. Eng.*, 2016, **1**, 272-279.
20. T. M. Floyd, M. A. Schmidt and K. F. Jensen, *Ind. Eng. Chem. Res.*, 2005, **44**, 2351-2358.
21. Y. W. Wang, Y. Y. Kim, H. K. Christenson and F. C. Meldrum, *Chemical Communications*, 2012, **48**, 504-506.
22. X. Gong, Y. W. Wang, J. Ihli, Y. Y. Kim, S. Li, R. Walshaw, L. Chen and F. C. Meldrum, *Adv Mater*, 2015, **27**, 7395-7400.
23. J. Ihli, W. C. Wong, E. H. Noel, Y. Y. Kim, A. N. Kulak, H. K. Christenson, M. J. Duer and F. C. Meldrum, *Nat Commun*, 2014, **5**, 3169.
24. C. N. R. Rao, *Chemical Applications of Infrared Spectroscopy*, Academic Press, London, 1963.
25. C. C. Tester, M. L. Whittaker and D. Joester, *Chemical Communications*, 2014, **50**, 5619-5622.
26. C. J. Stephens, S. F. Ladden, F. C. Meldrum and H. K. Christenson, *Adv. Funct. Mater.*, 2010, **20**, 2108-2115.
27. Y. W. Wang, H. K. Christenson and F. C. Meldrum, *Chemistry of Materials*, 2014, **26**, 5830-5838.
28. Y. W. Wang and F. C. Meldrum, *Journal of Materials Chemistry*, 2012, **22**, 22055-22062.
29. J. Ihli, Y. W. Wang, B. Cantaert, Y. Y. Kim, D. C. Green, P. H. H. Bomans, N. Sommerdijk and F. C. Meldrum, *Chemistry of Materials*, 2015, **27**, 3999-4007.
30. C. C. Tester, R. E. Brock, C.-H. Wu, M. R. Krejci, S. Weigand and D. Joester, *CrystEngComm*, 2011, 3975-3978.
31. C. J. Stephens, Y. Y. Kim, F. C. Meldrum and H. K. Christenson, *J. Am. Chem. Soc.*, 2011, **133**, 5210-5213.
32. C. Anduix-Canto, Y. Y. Kim, Y. W. Wang, A. Kulak, F. C. Meldrum and H. K. Christenson, *Crystal Growth & Design*, 2016, **16**, 5403-5411.
33. B. Cantaert, E. Beniash and F. C. Meldrum, *Chem. Eur. J.*, 2013, **19**, 14918-14924.
34. B. Cantaert, E. Beniash and F. C. Meldrum, *Journal of Materials Chemistry B*, 2013, **1**, 6586-6595.
35. W. B. Yue, A. N. Kulak and F. C. Meldrum, *Journal of Materials Chemistry*, 2006, **16**, 408-416.

36. W. B. Yue, R. J. Park, A. N. Kulak and F. C. Meldrum, *Journal of Crystal Growth*, 2006, **294**, 69-77.
37. Y. Y. Kim, N. B. J. Hetherington, E. H. Noel, R. Kroger, J. M. Charnock, H. K. Christenson and F. C. Meldrum, *Angewandte Chemie-International Edition*, 2011, **50**, 12572-12577.
38. E. Loste, R. J. Park, J. Warren and F. C. Meldrum, *Advanced Functional Materials*, 2004, **14**, 1211-1220.
39. Y.-W. Wang, H. K. Christenson and F. C. Meldrum, *Advanced Functional Materials*, 2013, **23**, 5615-5623.
40. Q. Jiang and M. D. Ward, *Chemical Society Reviews*, 2014, **43**, 2066-2079.
41. P. Cubillas and M. W. Anderson, in *Zeolites and Catalysis: Synthesis, Reactions and Applications*, eds. J. Čejka, A. Corma and S. Zones, Wiley VCH, Weinheim, Germany. , Editon edn., 2010.
42. E. Ruiz-Agudo and C. V. Putnis, *Mineralogical Magazine*, 2012, **76**, 227-253.
43. A. McPherson, A. J. Malkin and Y. G. Kuznetsov, *Annual Review of Biophysics and Biomolecular Structure*, 2000, **29**, 361-410.
44. E. H. H. Chow, D. K. Bucar and W. Jones, *Chemical Communications*, 2012, **48**, 9210-9226.
45. C. A. Orme, A. Noy, A. Wierzbicki, M. T. McBride, M. Grantham, H. H. Teng, P. M. Dove and J. J. DeYoreo, *Nature*, 2001, **411**, 775-779.
46. W. Habraken, J. H. Tao, L. J. Brylka, H. Friedrich, L. Bertinetti, A. S. Schenk, A. Verch, V. Dmitrovic, P. H. H. Bomans, P. M. Frederik, J. Laven, P. van der Schoot, B. Aichmayer, G. de With, J. J. DeYoreo and N. Sommerdijk, *Nature Communications*, 2013, **4**, 1507.
47. D. S. Li, M. H. Nielsen, J. R. I. Lee, C. Frandsen, J. F. Banfield and J. J. De Yoreo, *Science*, 2012, **336**, 1014-1018.
48. M. H. Nielsen, S. Aloni and J. J. De Yoreo, *Science*, 2014, **345**, 1158-1162.
49. J. N. Clark, J. Ihli, A. S. Schenk, Y.-Y. Kim, A. N. Kulak, J. M. Campbell, G. Nisbet, F. C. Meldrum and I. K. Robinson, *Nature Materials*, 2015, **14**, 780-784.
50. J. Ihli, J. N. Clark, A. S. Cote, Y. Y. Kim, A. S. Schenk, A. N. Kulak, T. P. Comyn, O. Chammas, R. J. Harder, D. M. Duffy, I. K. Robinson and F. C. Meldrum, *Nature Communications*, 2016, **7**.
51. F. Zaera, *Chemical Society Reviews*, 2014, **43**, 7624-7663.
52. E. Stavitski, M. H. F. Kox, I. Swart, F. M. F. de Groot and B. M. Weckhuysen, *Angewandte Chemie-International Edition*, 2008, **47**, 3543-3547.
53. M. J. Lardner, K. Y. Tu, S. M. Rosendahl, F. Borondics and I. J. Burgess, *Electrochimica Acta*, 2015, **162**, 72-78.

54. J. Karger, T. Binder, C. Chmelik, F. Hibbe, H. Krautscheid, R. Krishna and J. Weitkamp, *Nature Materials*, 2014, **13**, 333-343.